Planetary and Space Science 168 (2019) 1–14

Contents lists available at ScienceDirect

Planetary and Space Science

journal homepage: www.elsevier.com/locate/pss

Surface deposition of molecular contaminants in the mars 2020 rover wake

Jason Rabinovitch [*,1], Ira Katz [2]

Jet Propulsion Laboratory, California Institute of Technology, Pasadena, CA, 91109, USA

A B S T R A C T

The Mars 2020 rover has very strict contamination control requirements as it will cache samples on the surface of Mars for possible future return. It is known that the rover will outgas a minor amount of molecular contaminant on the surface of Mars, and numerical simulations using STAR-CCM+ are performed in order to predict the magnitude of the contaminant deposition to the Martian surface in the vicinity of the rover. Outgassing from the Rover Warm Electronics Bay (WEB) is predicted to be the dominant source of contamination for this scenario, and is therefore considered in this work. A flat terrain (i.e., no local topography) and a nominal rover orientation (i.e., no rocks under rover wheels, etc.) is also assumed. This analysis is performed in order to determine whether or not the M2020 rover WEB could self-contaminate a potential sampling site if the rover were to remain in the same location for an extended period of time. Simulations are performed under a variety of surface wind conditions, and it is determined that the predicted level of molecular contaminant deposition to the surface near the rover due to WEB outgassing and the model considered could be a maximum of 9 ng of organic contaminant in one specific location near the rover if the rover were to remain stationary for 100 sols.

1. Introduction

One of the primary scientific objectives of the next NASA planned Mars rover, Mars 2020 (M2020, Fig. 1), is to acquire and cache Martian surface samples for potential Mars sample return.[3] In order to ensure that Martian surface samples are not contaminated with Earth organic molecules that could degrade future science performed with the samples, an analysis is performed at the Jet Propulsion Laboratory (JPL), California Institute of Technology, that tracks potential contamination sources throughout all aspects of the M2020 mission. This contamination analysis is used to demonstrate that the M2020 rover will meet Level 1 contamination requirements. Possible contamination during spacecraft fabrication, assembly, launch, cruise, surface operations, and then a potential return trip to Earth is considered. As such, potential molecular contamination of sampling sites due to the proximity of the rover must be considered, and this work presents results from modeling possible molecular contamination of a drill site due to contaminants outgassing from the M2020 Rover during surface operations on Mars.

This paper provides an overview of the contamination requirements for the M2020 mission and the operational scenario of interest for this work, discusses the modeling approach and assumptions used, and then provides a discussion of the simulation results.

2. Background

This section provides an overview of the contamination requirements for the samples to be cached by the M2020 rover, and provides an overview of the contamination sources considered in this work. For scientific reasons, acceptable contamination levels for the acquired Mars samples are strict (e.g. (Summons et al., 2014; White et al., 2017)). Derived requirements state that the Total Organic Carbon (TOC) level of contamination per sample tube shall be less than 150 ng, and each sample tube and associated sampling site has a cross-sectional area of ~ 1.5 cm^2. A brief background of this requirement is discussed below, though it is not the objective of this work to provide context, and this work focuses on analyzing one scenario of interest that will contribute to the total amount of expected sample contamination during the M2020 mission.

2.1. Sample tube contamination requirement

The 150 ng limit for TOC is derived as follows - there is a Level 1 (L1) Requirement for Organic Cleanliness of Sample that states that the (e.g. (White et al., 2017), and Finding 6–12 from the 2013 Report of the Mars 2020 Science Definition Team[4]):

"Mars 2020 landed system shall be capable of encapsulating samples for return such that the organic contamination levels in each sample in

* Corresponding author.
E-mail address: jason.rabinovitch@jpl.nasa.gov (J. Rabinovitch).
[1] Engineer, Entry, Descent, & Landing and Formulation Group, 4800 Oak Grove Drive, M/S: T1708-112.
[2] Technologist, Principal, Propulsion, Thermal, & Material Systems Group, 4800 Oak Grove Drive, M/S: 125-109.
[3] https://mars.nasa.gov/mars2020/, accessed 10/20/2017.
[4] https://mars.nasa.gov/mars2020/files/mars2020/SDT-Report%20Finalv6.pdf.

https://doi.org/10.1016/j.pss.2018.12.009
Received 25 July 2018; Received in revised form 31 October 2018; Accepted 19 December 2018
Available online 24 December 2018

Nomenclature

D	Binary diffusion coefficient, m^2/s
$\hat{\mathbf{i}}, \hat{\mathbf{j}}, \hat{\mathbf{k}}$	Unit vectors in the x, y, and z directions, respectively
L	Characteristic length-scale, m
$M2020$	Mars 2020
$MMRTG$	Multi-Mission Radioisotope Thermoelectric Generator
MSL	Mars Science Laboratory
μ	Dynamic viscosity, kg/(m s)
$\tilde{\mu}$	Turbulent dynamic viscosity, kg/(m s)
ν	Kinematic viscosity, m^2/s
ϕ	Passive scalar volume fraction
$\widetilde{Pr}$	Turbulent Prandtl number
$RANS$	Reynolds-Averaged Navier-Stokes
Re	Reynolds number
ρ	Gas density, kg/m^3
Sc	Schmidt number
$\widetilde{Sc}$	Turbulent Schmidt number
θ	Angle of attack for free stream (wind direction), $^\circ$
TOC	Total Organic Carbon
U	Magnitude of characteristic free-stream velocity, m/s
WEB	Warm Electronics Bay
x_v, y_v	x and y coordinates of centroid of the two rover vents, m
y^+	Wall coordinate
z_g	z coordinate of ground plane, m

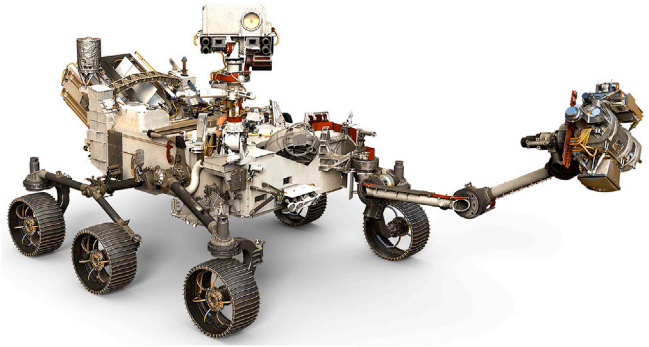

Fig. 1. Mars 2020 Rover rendering. The turret is seen on the right hand side of the image, and refers to the instruments and structure located at the end of the robotic arm. Photo credit: NASA (https://mars.nasa.gov/mars2020/mission/rover/, accessed 10/20/2017.).

the returned sample set are less than:

- Any Tier 1 compound (organic compounds deemed as essential analytes for mission success): 1 ppb
- Any Tier 2 compound (organic compounds not categorized as Tier 1): 10 ppb
- Total Organic Carbon: 10 ppb Baseline, 40 ppb Threshold"

Tier I compounds constitute those molecules that are likely to be most important to the science goals of the mission, i.e. those that could be indicative of martian and/or terrestrial life (e.g. all proteinogenic amino acids, common lipids, nucleotides, sugars, hydrocarbon biomarkers, etc.), and the second group (Tier II) comprises all other known organic molecules.[5]

In order to convert the 10 ppb organic carbon requirement to the 150 ng requirement, a nominal 15 g sample mass is assumed. This is consistent with an internal JPL requirement where an average rock core shall be $\geq$ 15 g with $\leq$10% of the rock cores being $<$ 10 g. Internally, allocations of this 150 ng requirement are allocated to different M2020 subsystems, so that the Mars 2020 project can track different contamination sources and determine if a specific subsystem is exceeding their specific contamination requirement or not.

2.2. Warm Electronics Bay contamination sources

Primarily due to warm electronics located inside of the rover in the Warm Electronics Bay (WEB), some amount of material outgassing of Tier 2 compounds is expected to occur while the M2020 Rover operates on Mars. There is a requirement stating that the outgassing rate shall be $<$ 100 ng/(cm^2 hour) from the WEB. All external rover surfaces have a much stricter outgassing requirement, at $<$ 1 ng/(cm^2 hour). Furthermore, the WEB is expected to be warm ($\sim 30^\circ$C), and external surfaces are not expected to be at temperatures $> -10^\circ$C for significant periods of time.[6] Based on a simple Arrhenius reaction rate approximation for outgassing rates, and due to the difference in requirements, a reduction of four orders of magnitude per unit area is expected for outgassing from the exposed rover surfaces compared to the WEB. Because of this, only the WEB is considered as an contaminant source in this work. This work focuses on determining if the WEB contaminants will deposit on the surface on a potential sampling site in order to relate the predicted amount of contaminant deposition from the WEB to contamination requirement discussed in the previous section (Sec. II.A.)

Fig. 2 depicts the basic operational scenario of interest for this work. When the rover is operating on Mars, molecular contaminants generated inside of the rover are expected to exit the rover chassis through two vents - one located on the aft end of the rover, and one located on the port side of the rover. Once the contaminants have left the confines of the rover chassis, they are expected to advect away from the rover due to surface winds, and to diffuse due to concentration gradients. Depending on wind direction and location of the rover, it is therefore possible for molecular contaminants to be deposited on a possible sampling site. Martian surface winds have been characterized during previous missions (for example, see (Hess et al., 1977; Murphy et al., 1990; Newman et al., 2017)), and experimentally measured wind speeds will serve as the foundation for the initial conditions chosen for this study. This work assumes a flat surface (no local topography), and a nominal rover geometry (no local rocks/slopes changing the rover orientation), as it is unknown what local features will be present at the actual landed location of the M2020 location.

If deemed necessary for scientific reasons, the M2020 Rover will loiter up to 100 sols near a potential sampling site of interest. If this happens, it is highly likely that the rover turret will be in the vicinity of the potential sampling site, so that the array of scientific instruments housed on the M2020 turret can be used to investigate the site of interest. Specifically, with the rover turret within 0.5 m of a potential coring site, the rover could possibly remain in the same location for up to 50 Martian sols, and up to 100 Martian sols for the turret within 10 m of a potential coring target. This operational configuration is the basis for the primary assumed geometry of the simulations presented in the following sections, where the wind primarily flows over the back of the rover towards the

[5] http://web.gps.caltech.edu/~als/research-articles/2014/final-report.pdf.

[6] http://www-k12.atmos.washington.edu/k12/resources/mars_data-information/data.html, accessed 11/12/2018.

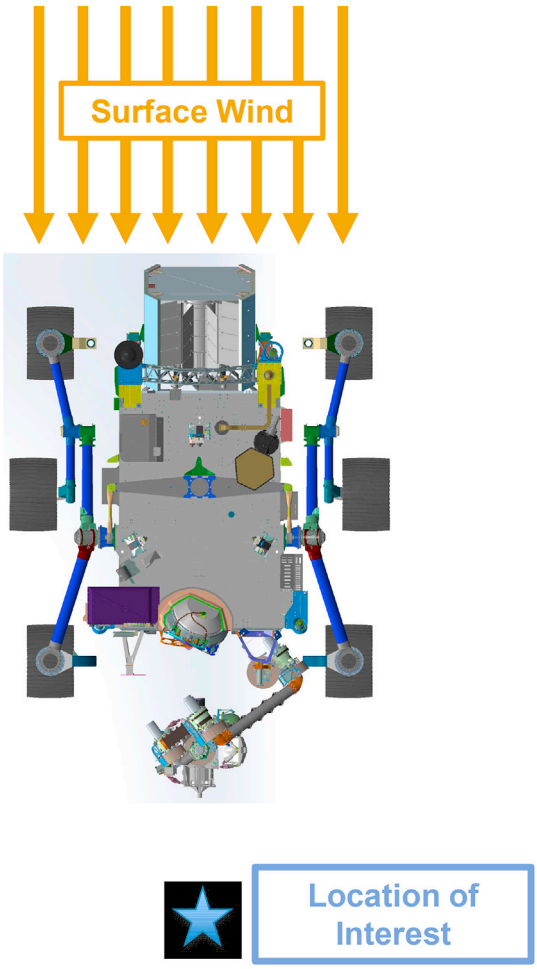

Fig. 2. General schematic of contamination scenario considered. In this schematic, a possible sampling site is directly downstream of the rover. However, this work looks at the predicted contamination deposited in a large area close to the rover and not just directly downstream, and also varies the direction of the surface wind.

deployed turret, which convects the contaminant closer to a possible sampling site, as shown in Fig. 2. Appendix A reproduces results presented in the main body of the paper for a rover geometry where the turret is in its stowed configuration (along the top-deck of the rover), to mimic the configuration of the rover during early phases of the surface mission, and to understand the sensitivity of the results to the geometry being considered.

Based on the predicted level of surface contamination from this work, it will be decided whether or not an operations requirement will have to be created to limit how long the rover can remain close to a possible sampling location before the sampling site is deemed to have been unacceptably contaminated by the rover.

3. Numerical model

The subject of passive scalar advection/diffusion in turbulent wakes is a field that contains a rich set of complex physics, and has been studied with great scientific rigor in the past (for example, see (Dimotakis, 2000; Holzer and Siggia, 1994; Shraiman and Siggia, 2000; Warhaft, 2000)). However, in this work, an engineering approximation is required to predict the amount of contaminant that will be deposited on the Martian surface in the vicinity of the M2020 rover, and the complex geometry of the rover itself and the asymmetric locations of the vents that act as sources for the contaminant (Fig. 3) introduce geometrical complications

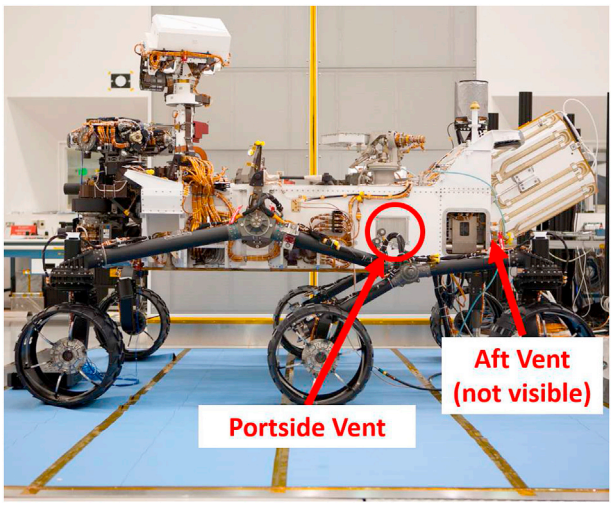

Fig. 3. Image of the MSL rover taken at NASA/JPL. The portside vent can clearly be seen, and the aft vent is located on the back of the rover, which is not visible in the image. These two vents are considered to be the only sources of a passive scalar for this work.

that are rarely considered in canonical research problems.

With these considerations in mind, the commercial CFD package STAR-CCM+[7] is used for this study. A steady state incompressible (density variations only due to temperature) coupled flow and energy solver is used for this work. The flowfield is solved concurrently with an advection/diffusion equation to model the transport of molecular contaminants near the rover, which is modeled numerically as a passive scalar. In order to account for small oscillations after convergence is achieved, results shown in this work have been averaged over 9000 iterations. Simple verification problems were solved originally (flow around a sphere and 1D unsteady diffusion) in order to ensure that the numerical methods were producing expected results for canonical problems. This section provides an overview of the numerical modeling approach used.

3.1. Numerical domain

Fig. 4 shows a schematic of the numerical domain used in this work. Standard M2020 spacecraft coordinates are used, such that the x-axis runs from the back to the front of the rover, with the aft end of the rover located on the $-x$ side, and the front of the rover (where the deployed turret is located) on the $+x$ side (Fig. 5). The origin of the coordinate system is located roughly at the centroid of the rover. A cylindrical domain is used, with the $-x$ curved surface being the inlet, and the $+x$ surface being the outlet. The ground plane, z_g, is located at $z_g = 1.13$ m, with the z-axis oriented in the direction of gravity. The y-axis is chosen to define a standard right-handed set of orthogonal coordinates. A top-plane is also included, though not shown in Fig. 4. Table 1 gives a summary of the numerical boundary conditions applied to the domain surfaces (see section III.B for a description of the rover boundary conditions used).

The numerical domain has a diameter of 50 m, which corresponds to ~ 25 characteristic rover lengths, as the M2020 rover is ~ 2 m x 2 m $\times$ 2 m. The height of the domain is 15 m. Therefore, the min/max spatial coordinates in the domain are x: [-25.0, 25.0] m, y: [-25.00, 25.00] m, and z: [-13.87, 1.130] m. This relatively large domain is used in order to minimize the effect that the boundaries will have on the flow field near the rover.

[7] https://mdx.plm.automation.siemens.com/star-ccm-plus, accessed 5/1/2018.

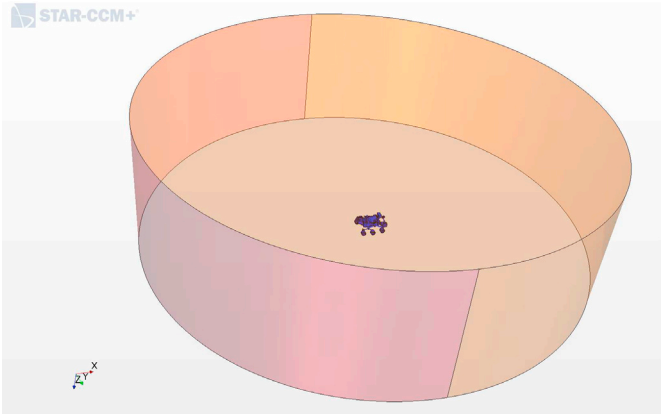

Fig. 4. Numerical domain used in this work. A 50 m diameter cylindrical domain is used in order to ensure that there is an adequate distance between the rover and domain boundary.

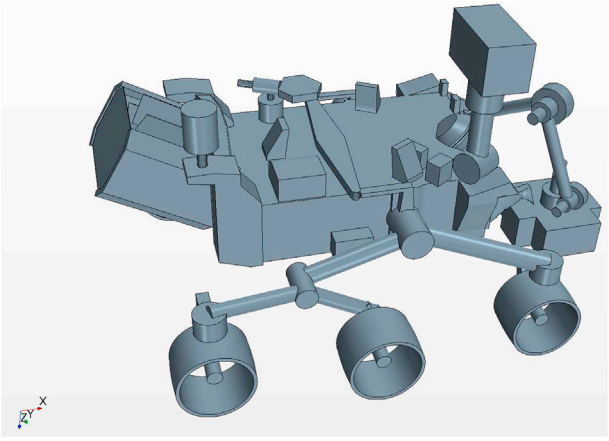

Fig. 5. Simplified M2020 rover model used for this work. All major components have been retained, though some of the small features seen in Figs. 1 and 3 have been ignored for computational considerations.

Table 1
Summary of numerical boundary conditions applied.

Surface	STAR-CCM+ Boundary	Parameters
Inlet	Velocity Inlet	Flow inlet with user specified velocity profile (see Sec. III.D)
Outlet	Pressure Outlet	Outlet surface with extrapolated backflow properties when needed
Ground Plane	Wall	No-slip adiabatic surface with a passive scalar concentration of 0
Top Plane	Pressure Outlet	Outlet surface with extrapolated backflow properties when needed

3.2. Rover geometry

A simplified M2020 rover model (Fig. 5) is used in order to retain all major components of the M2020 rover, yet reduce the amount of geometric complexity present so that the model is still numerically tractable. The majority of the surfaces of the rover are defined to be no-slip adiabatic walls with a specified passive scalar flux of zero. However, as M2020 is powered by a Multi-Mission Radioisotope Thermoelectric Generator (MMRTG), which converts heat into electrical power, some surfaces on the rover are expected to be hot, and these are discussed in Sec. III.B.1. The two vents, which are assumed to be the only sources of contamination in this work, are discussed in Sec. III.B.2.

3.2.1. Radioisotope thermoelectric generator (RTG) hot surface

The M2020 Rover will use the same MMRTG power source as the MSL Rover, which provides an electrical power output of approximately 110 W (Novak et al., 2015). While the temperature of the MMRTG is expected to vary based on local temperature (which can be landing site dependent), wind speed, di-urnal and seasonal variations, etc., in this work a constant isothermal temperature is assumed for the MMRTG cylinder and fins, as illustrated by Fig. 6. While MSL flight data (Novak et al., 2013; Cucullu et al., 2014) shows that MMRTG temperatures can vary significantly, a conservative bounding lower temperature of 115°C is chosen, which is well below any MSL observed temperatures. As the hot MMRTG induces a buoyant gas plume, this causes streamlines around the rover to move away from the Martian surface, which in turn convects possible contaminants away from the surface. Therefore, the hotter the MMRTG is, a lower amount of contamination will be deposited on the surface. Conversely, not accounting for MMRTG induced buoyancy could cause an nonphysical over-prediction of the amount of contaminant expected to be deposited on the Martian surface in the vicinity of the rover.

3.2.2. Contamination sources

As previously discussed, the WEB is the primary source of contamination considered in this study. There is a M2020 requirement (that will be verified via test) that the outgassing through the vents shall be less than 100 ng/(cm^2 hour). This worst-case value is used in this study, and worst-case outgassing is expected to occur when Mars surface temperatures, and subsequently WEB temperatures are high (relative to average Mars surface temperatures). All components of the M2020 Rover will go through bakeout cycles before launch in order to meet outgassing requirements. Because of this, it is assumed that only larger molecules outgas on Mars, as smaller molecules would have been depleted during earlier contamination bakeout processes (Stern et al., 1969).

Using transport properties given in (Bird et al., 1960), the binary diffusion coefficient, D, can be estimated for non-polar gases as a function of temperature and pressure. In this work, C_5H_{12} is conservatively chosen to have a characteristic molecular weight of a representative Tier 2 compound that can outgas from the WEB. Note that only the binary diffusion coefficient of the assumed contaminant is required for this analysis, and it is primarily driven by molecular weight. For the conditions assumed in this work, a binary diffusion coefficient of $6 \cdot 10^{-4}$ m^2/s into CO_2 is calculated. Temperature dependence of the binary diffusion coefficient is not accounted for in this work, as a large temperature gradient in the gas only exists in a small region away from the ground plane (Fig. 13). The contaminant is assumed to leave the rover chassis through two vents, shown for the numerical model in Fig. 7.

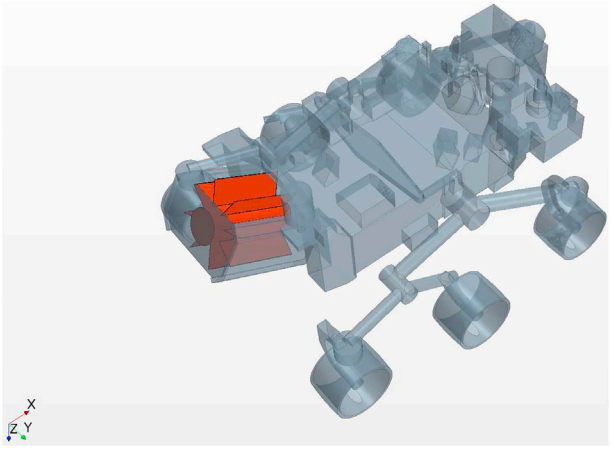

Fig. 6. Simplified M2020 rover model with MMRTG surfaces (115°C) shown in red. The rest of the rover model is made translucent to show the 3D nature of the MMRTG. (For interpretation of the references to color in this figure legend, the reader is referred to the Web version of this article.)

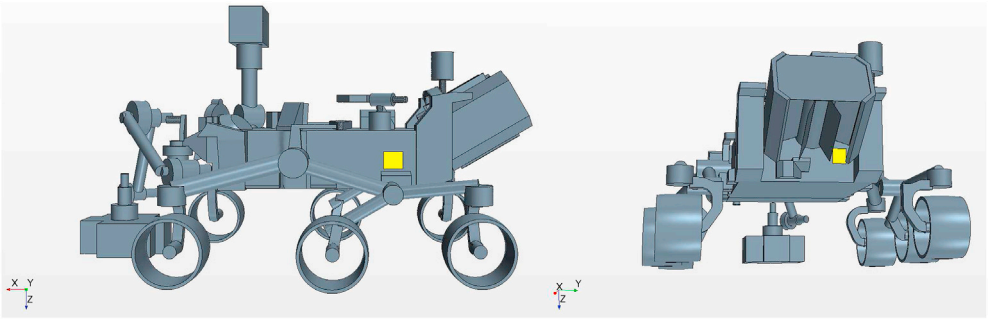

Fig. 7. Simplified M2020 rover model with vent surfaces shown in yellow (left: port vent, right: aft vent). These surfaces are contanimant (passive scalar) sources in the numerical simulations. (For interpretation of the references to color in this figure legend, the reader is referred to the Web version of this article.)

Due to the relatively low concentration levels of this contaminant in the flow (Fig. 15), the contaminant is modeled numerically as a passive scalar, with a volume fraction of ϕ. This assumes that the contaminant does not alter the bulk atmospheric gas properties in a significant manner so that a multi-component gas mixture does not have to be modeled numerically.

3.3. Meshes

The computational mesh used in this study is generated primarily to resolve the ground plane boundary layer, boundary layers over the rover surfaces, and the wake region behind the rover. The STAR-CCM+ polyhedral meshing algorithm is used in conjunction with a prism layer algorithm to generate all meshes used in this work. With the large numerical domain shown in Fig. 4, only two meshes are used to perform a pseudo-mesh refinement study. The first mesh contains $\sim 9.6 \cdot 10^6$ cells and the second, more refined mesh, contains $\sim 2.6 \cdot 10^7$ cells. For a characteristic free-stream velocity of 1.4 m/s, no significant difference in mass flux of contaminant to the ground is observed between the two meshes. However, as will be discussed in Sec. IV.A, in order to accommodate an increased free-stream velocity, and for consistency when comparing results, all results presented in later sections are generated using the most refined mesh. The refined rover surface mesh used is shown in Fig. 8, and the entire domain mesh with a center-plane cut is shown in Fig. 9.

3.4. Initial conditions

The physical scenario of interest for this work is a Martian surface wind blowing over the M2020 rover. In order to stay consistent with the assumed high WEB contaminant outgassing values, a relatively high ambient Mars temperature of 10° C (283 K) is assumed for this work. This high temperature also reduces the temperature difference between the free-stream and hot MMRTG surfaces. A free-stream pressure of 1070 Pa is assumed for a 100% CO_2 gas mixture. Using the ideal gas law, this results in a density of 0.02 kg/m^3. Based on previous measurements (for example (Mahaffy et al., 2013)), CO_2 is the primary constituent in the Mars atmosphere ($\sim$ 96% by volume). Neglecting the other trace species in this work will not have a significant effect on the quantities of interest being investigated as the gas bulk mixture properties are dominated by the CO_2 content. The standard Sutherland's law is assumed for dynamic viscosity and gas thermal conductivity, and a polynomial fit based on temperature is used for gas specific heat. The free-stream value for dynamic viscosity is $1.76 \cdot 10^{-5}$ Pa-s. Mars gravity is assumed to be 3.711 m/s^2, and due to the reference frame chosen for this work, gravity acts in the $+z$ direction.

A simple logarithmic wind boundary layer profile is assumed for this work with values extracted from viking wind data.[8] An inlet velocity profile of

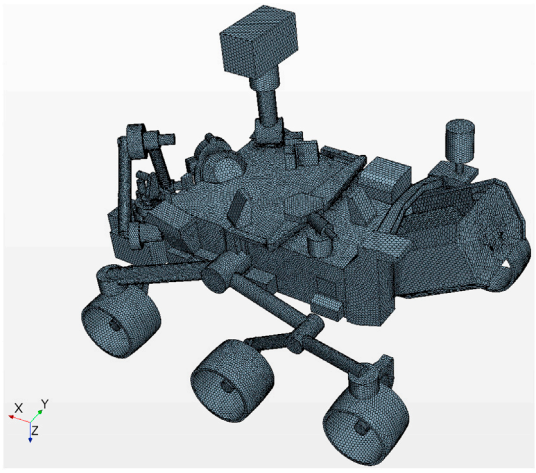

Fig. 8. Simplified M2020 rover model with the refined surface mesh shown.

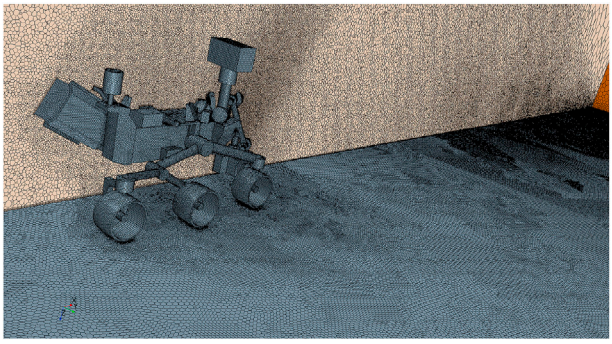

Fig. 9. Snapshot of overall domain with surface meshes shown on the rover, ground plane, domain outlet, and a center-plane section cut.

$$U(z) = U(z_{ref}) \frac{\log(|z - z_g|/z_0)}{\log(z_{ref}/z_0)} \quad (1)$$

is used, where $U(z)$ is the magnitude of the free-stream velocity, z_{ref} is a characteristic measurement height based on the Viking lander instrument suite (1.6 m), and z_0 is the surface roughness scale height, assumed to be 0.01 m in this work. As the wind speed on Mars is not constant, a variety of different values for $U(z_{ref})$ can be chosen.

Two different values of $U(z_{ref})$ are used in this work: 1.4 m/s and 5.0 m/s. 1.4 m/s corresponds to a $\sim$ 10% tile surface wind, and 5.0 m/s corresponds to a $\sim$ 65% tile wind based on Viking data. Depending on how far away from a potential sampling site the rover is, a low-speed or high-speed wind could provide a larger amount of contamination depo-

[8] http://www-k12.atmos.washington.edu/k12/resources/mars_data-information/data.html, accessed 5/3/2018.

sition to the area of interest. The direction of the free-stream is also varied in this work, though it is primarily aligned with the x-axis. The angle of attack, or wind direction (θ) is taken to be in the $x-y$ plane for this work (roll plane of the rover), with a positive θ defined to be a counter-clockwise rotation from the x-axis to the y-axis. With a positive angle of attack, the port-side vent moves closer to the stagnation point of the flow, and with a negative angle of attack the port-side vent moves closer to being in the rover wake. A summary of the initial conditions used for the flow is shown in Table 2.

3.5. Turbulence modeling

For characteristic velocities (U) of 1.4 m/s and 5.0 m/s, a characteristic length (L) of 2 m, a kinematic viscosity (ν) of $8.8 \cdot 10^{-4}$ m^2/s, the predicted Reynolds numbers ($Re = \frac{U \cdot L}{\nu}$) are $Re \simeq 1000$ and $Re \simeq 3000$ for the two different characteristic free-stream velocities, respectively. This puts the flow in a regime where an unsteady turbulent vortex street is expected to be observed in the wake (Lienhard, 1966). It should be noted that the local Re around different individual geometrical features is likely to be lower, i.e., if the characteristic lengthscale was chosen to be the mast diameter. However, these lower Re areas are still expected to generate an unsteady vortex street, though the flow may be in a transitional state.

Due to the engineering nature of this problem, both steady-state laminar and turbulent simulations were completed for the same initial conditions. Both the Realizable K-Epsilon Two-Layer Reynolds-Averaged Navier-Stokes (RANS) turbulence model and the SST(Menter) K-Omega RANS turbulence models were used in preliminary simulations with default coefficients, with meshes resolving $y^+ \simeq 1$. Simulations with the K-Epsilon model were found to predict the largest amount of contaminant mass deposition to the surface, so this model was used for all results presented in Sec. IV. Constant turbulent Prandtl ($\widetilde{Pr}$) and Schmidt ($\widetilde{Sc}$) numbers of 0.9 are assumed in the flow.

4. Results

This section provides a summary of results generated to date based on the initial conditions discussed in the previous section. Rover surface y^+ will be presented to give a quantitative measure of the mesh resolution attained in this study, and then both flow field properties and contaminant mass deposition results are showed.

4.1. Mesh size and computations

Figs. 10 and 11 show calculated y^+ values on the ground plane and rover surface for the refined mesh ($\sim 2.6 \cdot 10^7$ cells) for characteristic free-stream velocities of 1.4 m/s and 5.0 m/s, respectively. An θ of 0° is used in both of these cases. The maximum y^+ values observed on the rover are 1.9 and 3.7 for the two different free-stream velocities. y^+ values > 1 are generally only seen in local stagnation regions and in areas where flow separation is expected to occur, which gives confidence in the mesh resolution used. Computations are run locally at JPL using 240 cores on the Zodiac cluster. After 1000 iterations (when a converged solution is reached), the results presented below are averaged over 9000 additional iterations. While less relevant when RANS turbulence models are being used, with preliminary laminar simulations, oscillations were observed in the solution (likely due to unsteady vortex shedding), and an average solution over several flow cycles was desired in order to give a relevant averaged result. These oscillations in residuals are generally not seen once a turbulence model is enabled.

Table 2
Summary of initial fluid conditions used.

Property	Value(s)
Temperature (K)	283
Pressure (Pa)	1070
Density (kg/m^3)	0.02
$U(z_{ref})$ (m/s)	1.4, 5.0
θ (°)	0, ±5, ±15, ±30

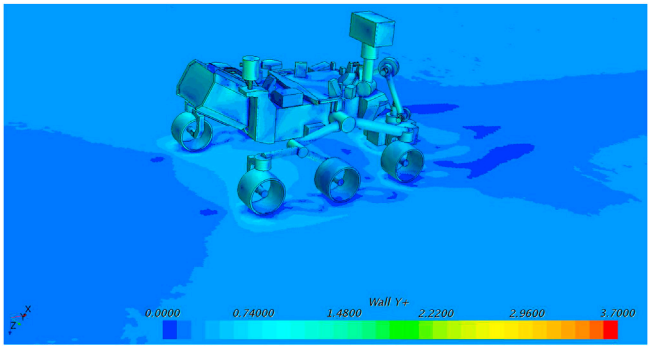

Fig. 10. Contour plot showing calculated y^+ values on the ground plane and rover surface for $U(z_{ref}) = 1.4$ m/s, and 0° angle of attack.

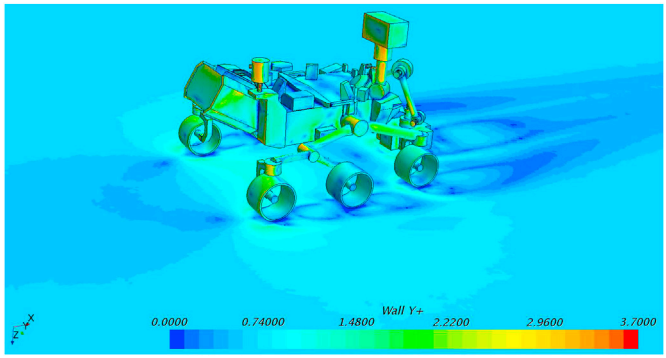

Fig. 11. Contour plot showing calculated y^+ values on the ground plane and rover surface for $U(z_{ref}) = 5.0$ m/s, and 0° angle of attack.

4.2. Flow field

For brevity, this section only shows sample results for a free-stream characteristic velocity of 5.0 m/s, and a 0° angle of attack. Fig. 12 shows velocity vectors colored by velocity magnitude along the center-plane of the domain which means that the three-dimensional nature of the flow field is not shown. As expected, re-circulation zones are visible near the rover top-deck and behind the deployed turret. Fig. 13 shows the relatively small region where the gas temperature has increased due to the hot RTG surfaces in the simulation. A cut of the center-plane of the domain is shown where the gas temperature is between 284 K and 388 K. The hot MMRTG surface is shown in red.

Qualitatively, varying the angle of attack of the flow and flow velocity does not change the major features observed in the flow solution (standard bluff body flow phenomena). However, and this will be discussed in more detail in the next section, due to the complex geometry of the rover and the location of the vents, the overall deposition of contaminant to the surface is sensitive to streamlines near the vents traveling either under the rover chassis or over the rover top-deck. If these streamlines, which generally correspond to regions of the flow with a relatively high concentration of contaminant, travel beneath the rover, then the contamination is convected closer to the ground plane, which will increase the mass deposition levels observed in the rover wake.

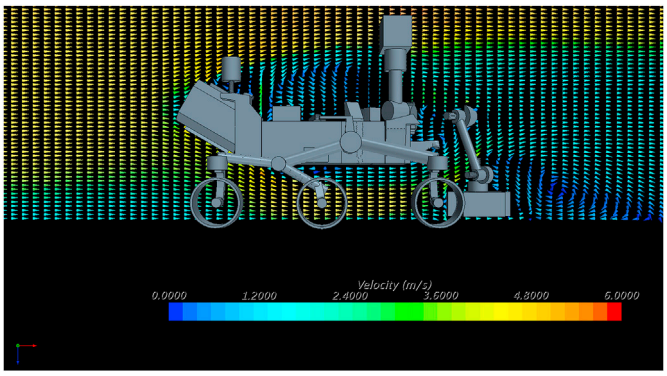

Fig. 12. Mean velocity vectors colored by velocity magnitude along the center-plane of the domain for $\theta = 0^{\circ}$ and $U(z_{ref}) = 5.0$ m/s. Two primary re-circulation regions above the rover deck and downstream of the turret can be seen.

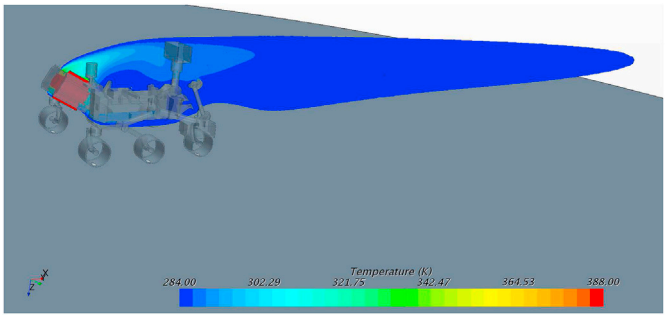

Fig. 13. Gas temperature along the center-plane of the numerical domain for $\theta = 0^{\circ}$ and $U(z_{ref}) = 5.0$ m/s. The gas temperature contour is clipped so that only areas of the flow with 284 K$\leq T \leq$ 388 K are shown. The hot RTG surface is shown as well.

4.3. Contamination concentrations and mass deposition

The quantity of interest in this study is the mass flux of the passive scalar (molecular contaminant) to the surface. As discussed previously, the ground plane has a boundary condition set to 0 concentration of passive scalar, which means that no contaminant accumulates on the surface. The magnitude of the diffusion mass flux to the surface ($\dot{m}$) is desired, which can be calculated from

$$\dot{m} = -\left(\frac{\mu}{Sc} + \frac{\tilde{\mu}}{\widetilde{Sc}}\right)\nabla\phi \cdot \hat{\mathbf{k}}, \tag{2}$$

where μ is the dynamic viscosity, $\tilde{\mu}$ is the turbulent viscosity, and $\hat{\mathbf{k}}$ is the unit vector in the z direction. The mass flux due to convection is 0 due to the ground plane being a no-slip/no-penetration wall, and in the coordinate system used, $\dot{m}$ should be positive when mass is deposited on the surface. The mass diffusion flux has standard units of kg/(m^2 s), though for the majority of the rest of this work, results will be presented using units of ng/(cm^2 sol) in order for comparisons relevant to M2020 time-scales and length scales to be made in a simple manner. One Martian sol (day) is taken to be 24 h, 39 min, and 35.244 s. Due to the low value of the binary diffusion coefficient of the contaminant under Mars conditions as well as the relevant length scales and time scales of the problem, turbulent mixing drives the evolution of the contaminant field, and not pure mass diffusion.

Figs. 14 and 15 show streamlines emanating from the contaminant vent surfaces as well as the concentration of the contaminant along the center-plane of the domain for the 5 m/s characteristic free-stream velocity with 0° angle of attack. The ground plane is colored by predicted mass deposition to the surface. Some streamlines travel beneath the rover which indicates that some of the contaminant is initially convected close to the surface, which causes an increased amount of contaminant to be deposited to the surface.

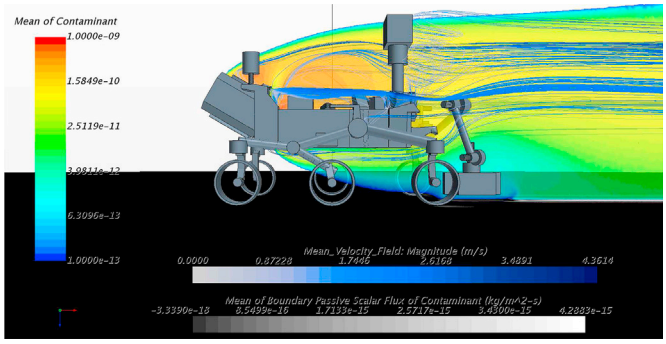

Fig. 14. Simulation results for $\theta = 0^{\circ}$ and $U(z_{ref}) = 5.0$ m/s. Streamlines eminating from the rover vents and contaminant concentration along the center-plane is shown. It is possible to see some of the streamlines which travel under the rover and closer to the surface.

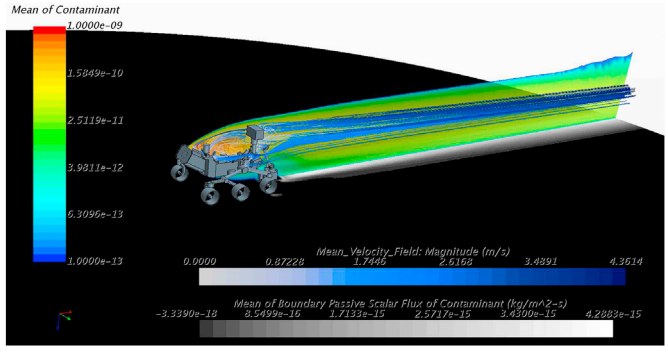

Fig. 15. Simulation results for $\theta = 0^{\circ}$ and $U(z_{ref}) = 5.0$ m/s. Streamlines eminating from the rover vents and contaminant concentration along the center-plane is shown. A relatively small growth in the vertical direction of the contaminant profile is seen downstream due to the relatively small amount of molecular diffusion occurring before the flow exits the domain.

Sample mass deposition contour plots for a characteristic free-stream velocity of 5 m/s, and wind angles of −30°, 0°, and 30°, are shown in Figs. 16–18. STAR-CCM+ results generated on an unstructured grid are linearly interpolated onto a cartesian grid with equal spacing, with 501 points in each of the x and y directions. Dashed circles are plotted at a radius of 5 m and 10 m from the center of the rover for scale. The direction of the free-stream is also shown, and an approximate rover outline (with vents indicated) is shown in green.

In order to compare the effect of free-stream angle of attack on the two wind speeds considered, Figs. 19 and 20 show cumulative mass deposition (not flux) values as a function of radius (calculated to ensure conservation of mass in the domain). Radius is defined as the distance to the origin based on the centroid of the two vents, with $r = \sqrt{(x - x_c)^2 + (y - y_c)^2}$. High angle of attack flows (both in the positive and negative direction) generally have the highest total mass depositions to the surface. This is primarily attributed to the location of the port vent; for the $\theta = \pm 30^{\circ}$ wind directions, the port-side vent is located closer to either the wake or the stagnation region of the rover (compared to the 0° wind direction). With this flow/rover alignment, the port-vent streamlines, and therefore contaminant, are convected closer to the ground, which ends up increasing the level of mass deposition for these wind angles.

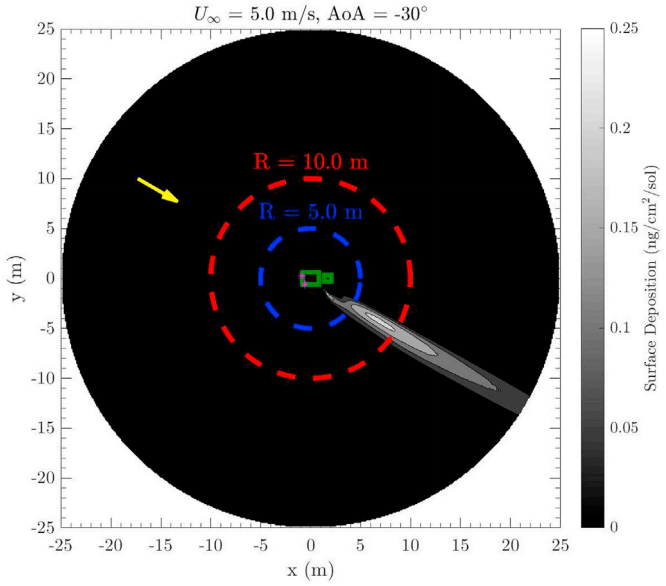

Fig. 16. Predicted contaminant surface mass deposition contour plot for $\theta = -30^{\circ}$ and $U(z_{ref}) = 5.0$ m/s. The free-stream direction is shown by the yellow arrow, and an approximate outline of the rover and turret is shown in green (with vents noted). Circles showing 5 m and 10 m distances from the origin. (For interpretation of the references to color in this figure legend, the reader is referred to the Web version of this article.)

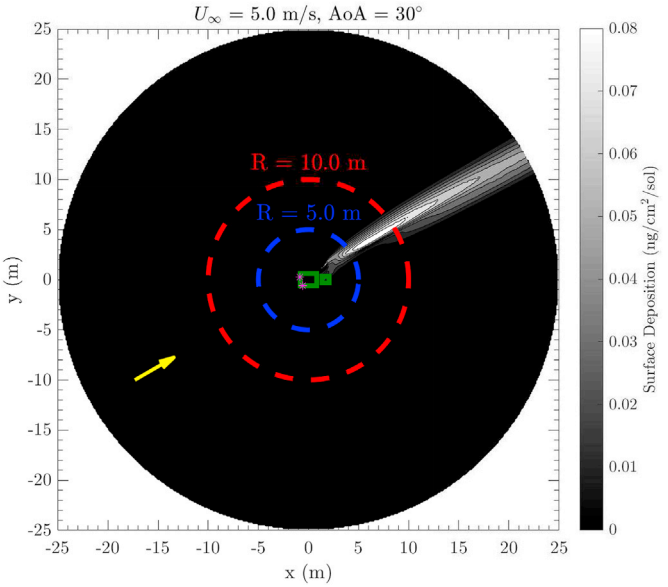

Fig. 18. Predicted contaminant surface mass deposition contour plot for $\theta = 30^{\circ}$ and $U(z_{ref}) = 5.0$ m/s. The free-stream direction is shown by the yellow arrow, and an approximate outline of the rover and turret is shown in green (with vents noted). Circles showing 5 m and 10 m distances from the origin are shown for scale. (For interpretation of the references to color in this figure legend, the reader is referred to the Web version of this article.)

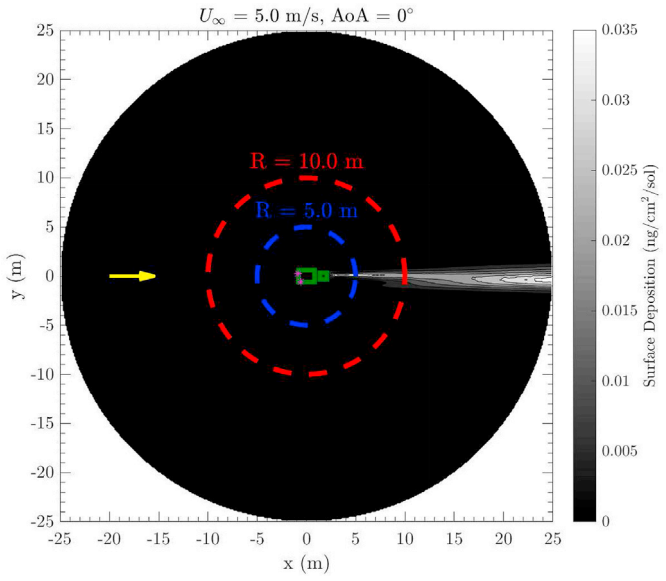

Fig. 17. Predicted contaminant surface mass deposition contour plot for $\theta = 0^{\circ}$ and $U(z_{ref}) = 5.0$ m/s. The free-stream direction is shown by the yellow arrow, and an approximate outline of the rover and turret is shown in green (with vents noted). Circles showing 5 m and 10 m distances from the origin are shown for scale. (For interpretation of the references to color in this figure legend, the reader is referred to the Web version of this article.)

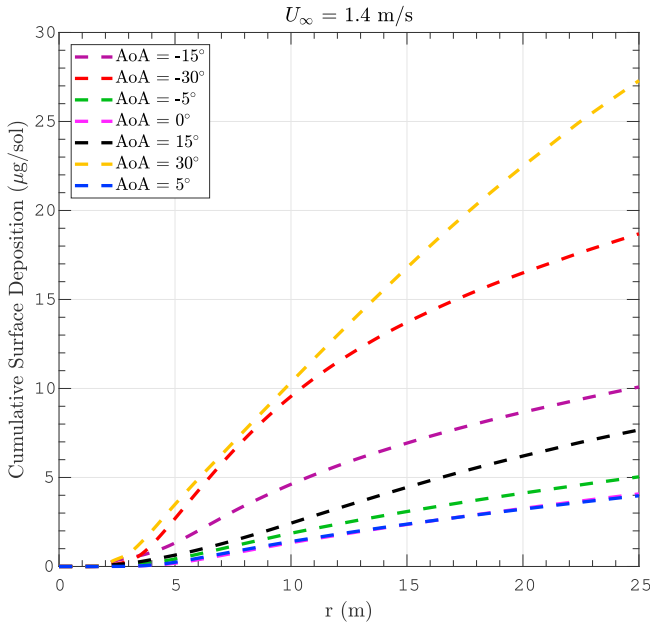

Fig. 19. Cumulative contaminant deposition profiles as a function of radius for $U(z_{ref}) = 1.4$ m/s.

4.4. Spatial averaging

As shown in (Newman et al., 2017), MSL has measured significant variance in both wind direction and speed throughout its mission thus far. The simulations presented so far have only been for discrete wind directions and velocities. In order to evaluate the potential contamination risk to a drill site due to the M2020 rover loitering in a single location, timescales on the order of 50 or 100 sols are of interest. This implies that some spatial averaging of the results presented in the previous section should be performed in order to account for the constantly changing Martian surface winds.

The wind environment that the M2020 rover will experience is expected to be influenced by many factors, including (but not limited to) seasonal variations, diurnal effects, and geographic effects (both depending on landing site selection, and local terrain features). Due to impracticality of trying to model all of these complex phenomena, a

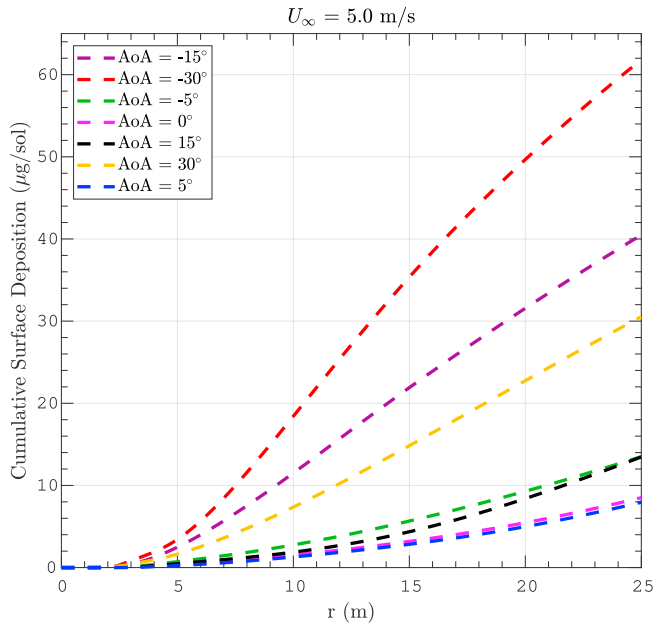

Fig. 20. Cumulative contaminant deposition profiles as a function of radius for $U(z_{ref}) = 5.0$ m/s.

simplified approach is taken.

Wind direction (angle of attack) variability is modeled using a normal distribution with a probability density given by

$$f(\theta) = \frac{1}{\sqrt{2\pi\sigma^2}} e^{\frac{-(\theta-\xi)^2}{2\sigma^2}}, \tag{3}$$

where θ is the wind direction being considered, ξ is the mean wind angle, and σ is the standard deviation of the wind direction in degrees. While data in (Newman et al., 2017) shows a relatively large angle variability in wind direction, here a conservative standard deviation of 15° is assumed.

Discrete numerical results now need to be spatially averaged while still conserving mass from the original simulation results. The algorithm used in this work is first described assuming only one numerical simulation at θ_o has been completed, and then is extended to incorporate results from multiple numerical simulations at multiple angles. θ is linearly discretized, where $\theta = [\theta_1, \theta_2, \ldots, \theta_i, \ldots, \theta_{n-1}, \theta_n]$, where $n = 1000$, $\theta_1 = \xi - 6\sigma$ and $\theta_n = \xi + 6\sigma$. In order to enforce discrete mass conservation, a numerical weighting coefficient, ψ, is used to ensure $\sum_{i=1}^{n} \psi f(\theta_i) = 1$.

Let $\dot{m}_{n,\theta}(x,y)$ correspond to original numerical results for a wind angle of θ linearly interpolated onto an equally spaced cartesian mesh, still with units of ng/(cm^2 sol). In order account for wind vaiability, let $\overline{m}_{\xi,\sigma}(x,y)$ correspond to the averaged contaminant mass flux field for a mean wind angle of ξ and a wind direction standard deviation of σ. Therefore, a spatially averaged contaminant deposition field can be represented by

$$\overline{m}_{\xi,\sigma}(x,y) = \sum_{i=1}^{n} \psi f(\theta_i) \dot{m}_{\theta_i}(x,y). \tag{4}$$

However, in this example, numerical results are only available for $\theta = \theta_o$, i.e., $\dot{m}_{n,\theta_o}(x,y)$. To account for this, $\dot{m}_{\theta_i}(x,y)$ is calculated by a solid-body rotation of the original $\dot{m}_{n,\theta_o}(x,y)$ solution by a rotation angle, θ_r, where $\theta_r = \theta_i - \theta_o$. With $x = rcos(\theta)$ and $y = rsin(\theta)$, then $\dot{m}_{\theta_i}(x,y) = \dot{m}_{n,\theta_o}(cos(\theta_r)x + sin(\theta_r)y, -sin(\theta_r)x + cos(\theta_r)y)$ Numerically, this is accomplished using 2D linear interpolation of the original numerical solution.

As multiple numerical simulations have been completed, it is possible to combine these results for a given θ_i. For example, assume that numerical simulations have been completed at angles θ_α and θ_β, and $\theta_\alpha < \theta_i < \theta_\beta$. In this scenario, $\dot{m}_{n,\theta_i}(x,y)$ is calculated by rotating $\dot{m}_{n,\alpha}(x,y)$ by $\theta_r = \theta_i - \theta_\alpha$ and by rotating $\dot{m}_{n,\beta}(x,y)$ by $\theta_r = \theta_i - \theta_\beta$ and then summing the two resulting rotated contaminant mass flux fields using appropriate weighting coefficients based on a linear interpolation in θ. I.e., $\dot{m}_{n,\theta_i}(x,y) = \Gamma_l \dot{m}_{n,\alpha}(x,y) + \Gamma_r \dot{m}_{n,\beta}(x,y)$, where $\Gamma_l = \frac{\theta_i - \theta_\alpha}{\theta_\beta - \theta_\alpha}$ and $\Gamma_r = \frac{\theta_\beta - \theta_i}{\theta_\beta - \theta_\alpha}$, and $\Gamma_l + \Gamma_r = 1$ by construction.

If θ_i is outside of the range of numerical simulations completed ($\theta_i < -30^\circ$ or $\theta_i > 30^\circ$ for this study), then no linear interpolation is used, and the numerical results with $\theta = \pm 30^\circ$ are rotated accordingly. With this algorithm, simulations with differing characteristic free-stream velocities are analyzed separately.

Figs. 21–26 show this method for a characteristic free-stream velocity of 1.4 m/s, $\xi = [-30^\circ, 0^\circ, 30^\circ]$, and $\sigma = 15^\circ$, and results for a characteristic free-stream velocity of 5.0 m/s, once again with $\xi = [-30^\circ, 0^\circ, 30^\circ]$ and $\sigma = 15^\circ$. Fig. 27 shows results for a characteristic free-stream velocity of 5.0 m/s, with $\xi = -30^\circ$ and $\sigma = 15^\circ$, but focusing only on the surface within a 3 m radius of the origin, showing the small amount of contaminant predicted to be deposited to the surface close to the rover.

5. Discussion

Even with the conservative assumptions used in this work, the predicted mass deposition of contaminant to the surface in the vicinity of the M2020 is relatively low. In terms of a localized predicted peak deposition, Fig. 24 shows a localized maximum value of ~ 0.06 ng/(cm^2 sol). If a Mars surface wind maintained the same velocity, mean angle, and relatively narrow direction variance continuously for 100 sols, then a maximum of 9 ng of organic contaminant could accumulate on a potential sampling site with a size of 1.5 cm^2. This is only 6% of the original 150 ng (Sec. II.A) contaminant budget per cached sample, and can easily be accommodated in the overall contaminant budget. This local maximum also only occurs at one discrete point in the domain, with the rest of the domain predicting significantly less contaminant deposition onto the surface. This maximum deposition value bounds the results shown in Appendix A which considers a second geometry where the rover turret is in a stowed configuration.

Furthermore, a strong diurnal effect is expected to be seen with wind direction, and the wind is expected to change by ~ 180° between a

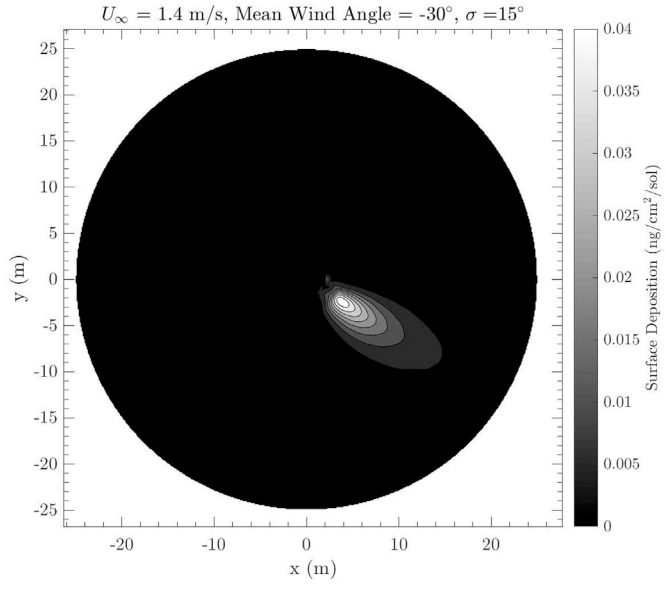

Fig. 21. Spatially averaged predicted contaminant surface mass deposition contour plot for $U(z_{ref}) = 1.4$ m/s, $\xi = -30^\circ$, and $\sigma = 15^\circ$.

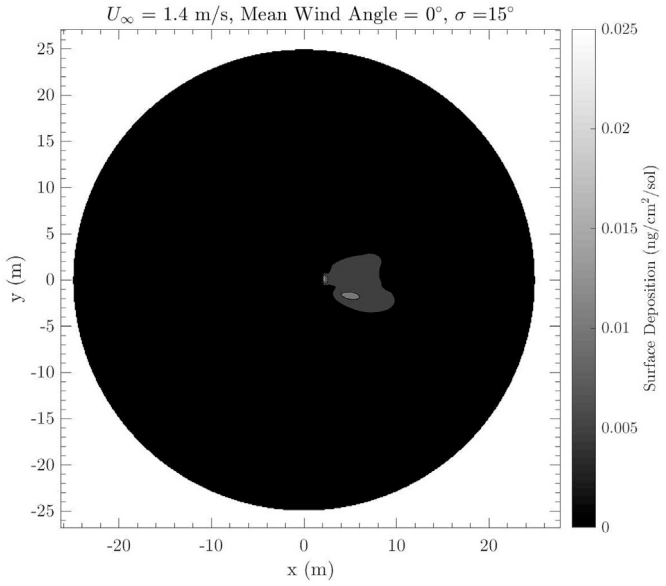

Fig. 22. Spatially averaged predicted contaminant surface mass deposition contour plot for $U(z_{ref}) = 1.4$ m/s, $\xi = 0^{\circ}$, and $\sigma = 15^{\circ}$.

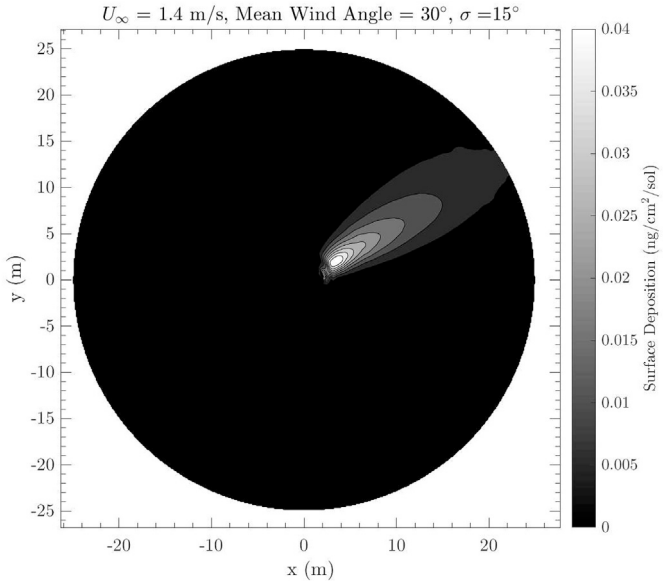

Fig. 23. Spatially averaged predicted contaminant surface mass deposition contour plot for $U(z_{ref}) = 1.4$ m/s, $\xi = 30^{\circ}$, and $\sigma = 15^{\circ}$.

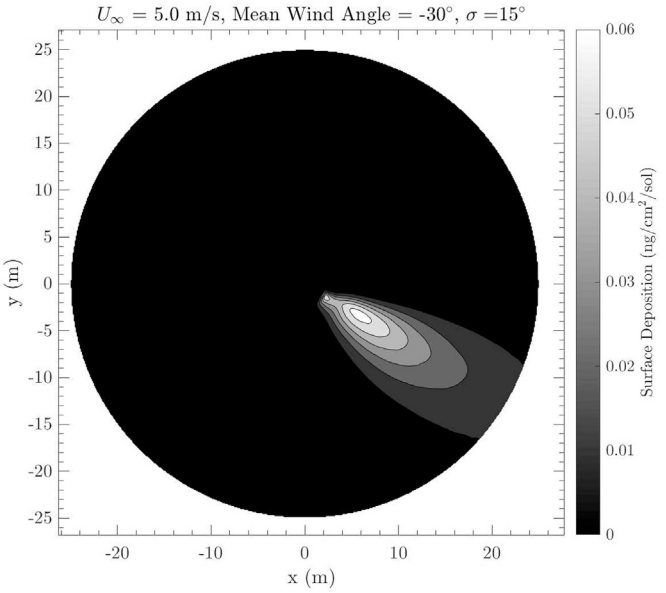

Fig. 24. Spatially averaged predicted contaminant surface mass deposition contour plot for $U(z_{ref}) = 5.0$ m/s, $\xi = -30^{\circ}$, and $\sigma = 15^{\circ}$.

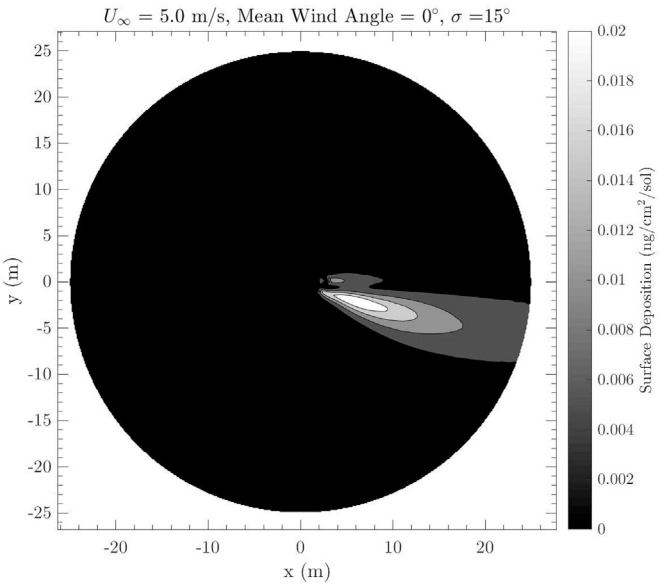

Fig. 25. Spatially averaged predicted contaminant surface mass deposition contour plot for $U(z_{ref}) = 5.0$ m/s, $\xi = 0^{\circ}$, and $\sigma = 15^{\circ}$.

Martian day and night. This would generate a bi-modal wind direction distribution, further reducing the predicted contaminant mass deposition in the areas downstream of the rover. It is expected that local topography will have a large effect on the preferential wind direction experienced by the rover at a specific location, but a standard deviation of 15° is a small change in angle when compared to many of the MSL measurements (Newman et al., 2017). If σ is increased, than the predicted contaminant deposition is expected to decrease linearly with σ.

The results presented used a binary diffusion coefficient for C_5H_{12} under Martian conditions. Using (Bird et al., 1960), D can be easily calculated for linear alkanes of C_4H_{10} through under Martian conditions. Using a simple exponential fit for D gives the relation C_9H_{10}, where $D = 0.0071 \cdot M_w^{-0.594}$ is the M_w molecular weight of the species being considered in AMU, and the other two constants are consistent with D having units of m^2/s. The larger the hydrocarbon, the lower the binary diffusion coefficient. Decreasing the value of D used in the numerical simulations will decrease the predicted surface deposition of contaminant, as the first term in Eq. (2) is proportional to D.

While results for only two characteristic free-stream velocities have been presented in detail in this work, Figs. 28 and 29 show the predicted contaminant deposition for $\alpha = 0^{\circ}$ and $\alpha = -30^{\circ}$, for a characteristic free-stream velocity of 10 m/s, respectively. As the mesh was not changed for these simulations, increasing $y+$ values make it difficult to directly resolve all boundary layers, and more reliance is placed on the RANS turbulence model used. However, a significant reduction in contaminant deposition is observed in the domain when compared to Fig. 17, and a small decrease is seen comparing to 16. This indicates that the increased free-stream velocity is convecting the contaminant farther downstream, and out of the area of interest before being potentially deposited on the surface. If desired, it would be possible to combine

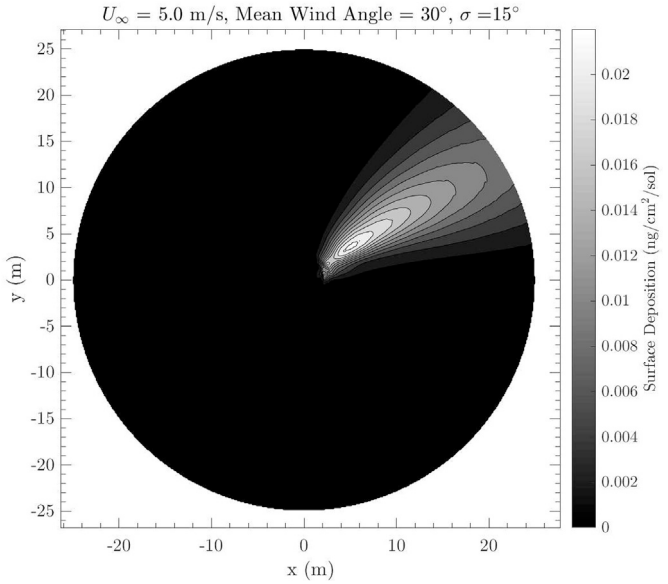

Fig. 26. Spatially averaged predicted contaminant surface mass deposition contour plot for $U(z_{ref}) = 5.0$ m/s, and $\xi = 30^{\circ}$.

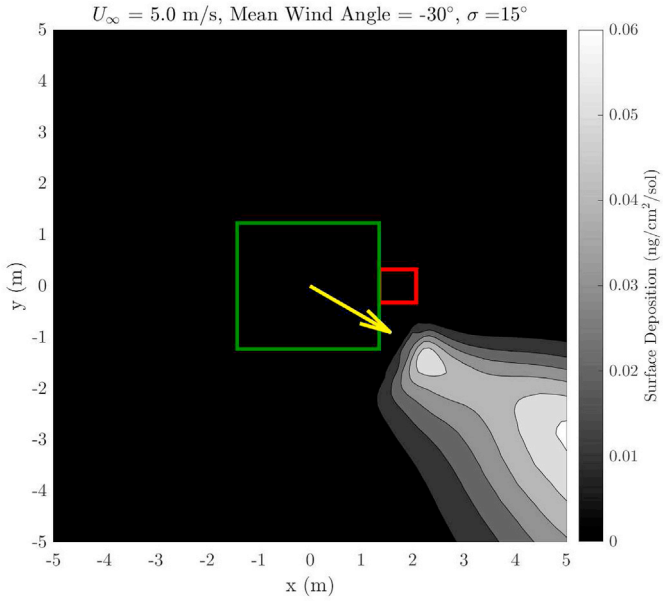

Fig. 27. Spatially averaged predicted contaminant surface mass deposition contour plot for $U(z_{ref}) = 5.0$ m/s, $\xi = -30^{\circ}$, and $\sigma = 15^{\circ}$ focusing on a region close to the rover. Approximate rover outline and freestream direction indicated in figure.

simulation results performed with different free-stream velocities and interpolating between them assuming a Weibull distribution for wind velocity, which has been used in the past (Lorenz, 1996, 2016).

6. Conclusions

A variety of numerical simulations were run to investigate the possibility of a molecular contaminant from the M2020 Rover WEB contaminating a potential sampling site in the vicinity of the rover. The molecular contaminant was modeled numerically as a passive scalar, and a spatial averaging process was used to conservatively account for some of the wind variability expected to occur on the surface of Mars. A flat surface (no local topography) and a nominal simplified rover geometry

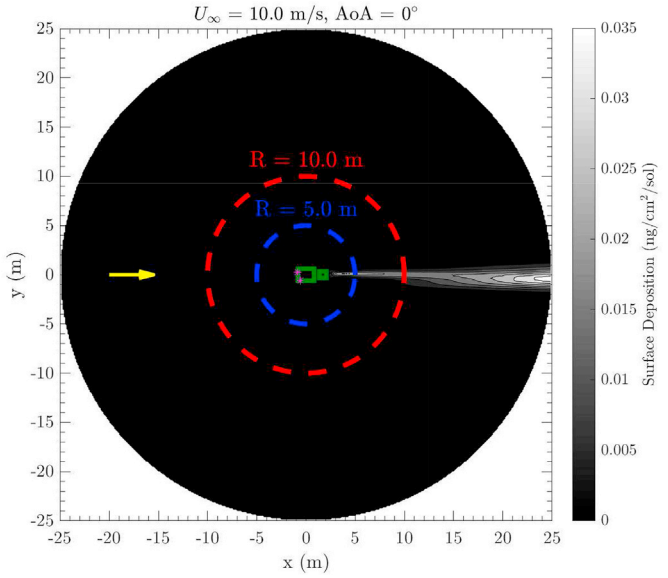

Fig. 28. Predicted contaminant surface mass deposition contour plot for $\alpha = 0^{\circ}$ and $U(z_{ref}) = 10.0$ m/s. The free-stream direction is shown by the yellow arrow, and an approximate outline of the rover and turret is shown in green (with vents noted). Circles showing 5 m and 10 m distances from the origin are shown for scale. (For interpretation of the references to color in this figure legend, the reader is referred to the Web version of this article.)

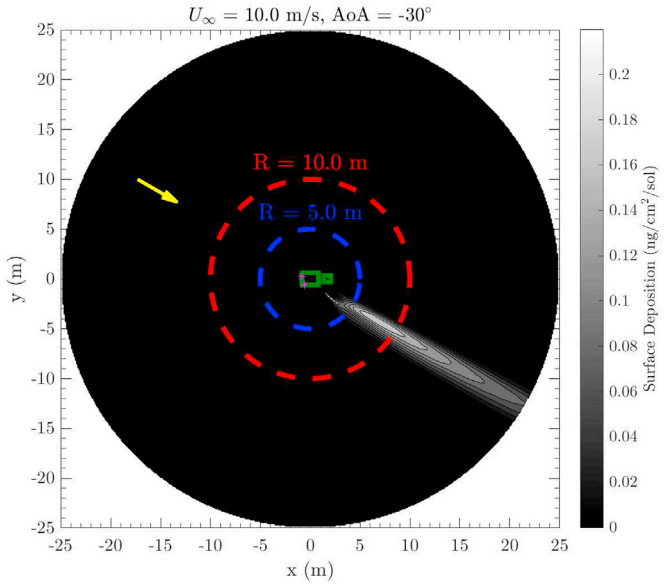

Fig. 29. Predicted contaminant surface mass deposition contour plot for $\alpha = -30^{\circ}$ and $U(z_{ref}) = 10.0$ m/s. The free-stream direction is shown by the yellow arrow, and an approximate outline of the rover and turret is shown in green (with vents noted). Circles showing 5 m and 10 m distances from the origin are shown for scale. (For interpretation of the references to color in this figure legend, the reader is referred to the Web version of this article.)

was considered for this work. With potentially long rover loiter times on Mars (50 sols for the turret within 0.5 m of a potential sampling site, and 100 sols for the turret within 10 m of a potential sampling site), for the model considered, the predicted surface contaminant deposition values are well within acceptable levels, and do not constitute a major component of the 150 ng/sample requirement accepted by the M2020 mission.

Funding

The research was carried out at the Jet Propulsion Laboratory, California Institute of Technology, under a contract with the National Aeronautics and Space Administration. U.S. Government sponsorship acknowledged.

Acknowledgments

The research was carried out at the Jet Propulsion Laboratory, California Institute of Technology, under a contract with the National Aeronautics and Space Administration. The authors would like to acknowledge the CAD support of Eddie Ketsiri, Carlee Wagner (Siemens) for STAR-CCM+ support, and the rest of the M2020 Contamination Control team for their support. The decision to implement Mars Sample Return will not be finalized until NASA's completion of the National Environmental Policy Act (NEPA) process. This document is being made available for information purposes only.

Appendix A. Supplementary data

Supplementary data to this article can be found online at https://doi.org/10.1016/j.pss.2018.12.009.

Appendix

A.Summary of Stowed Turret Results

This appendix contains a summary of the results obtained using a rover geometry where the turret is stowed. This is the configuration of the rover immediately after landing on the surface of Mars. The turret is deployed after standard checkouts are performed in order to ensure that the rover is healthy and operating correctly on the Martian surface.

Fig. 30 shows a geometrical comparison of the two rover models (direct comparision to Fig. 5) showing the turret head located on the top deck of the rover. The mesh used in this domain uses the same characteristic dimensions as the fine mesh reported previously, and contains $\sim 2.5 \cdot 10^7$ cells. The rest of the numerical domain is the same as reported in Sec. III.A. Fig. 31 shows the mean velocity profile for the rover (direct comparison to Fig. 12 for a characteristic free stream velocity of 5 m/s and $\theta = 0^{\circ}$.

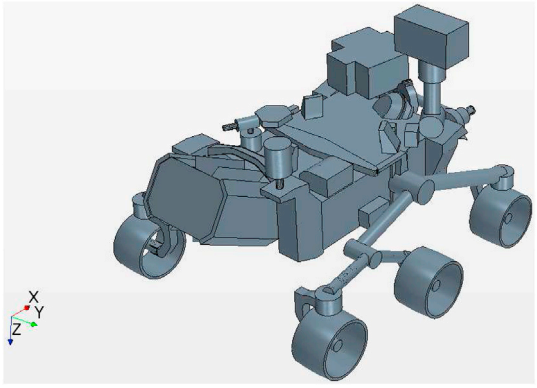

Fig. 30. Simplified M2020 rover model used with the turret in the stowed configuration. All additional components of the model (vents, MMRTG, boundary conditions, domain etc.) are consistent with the results presented in the main body of this work.

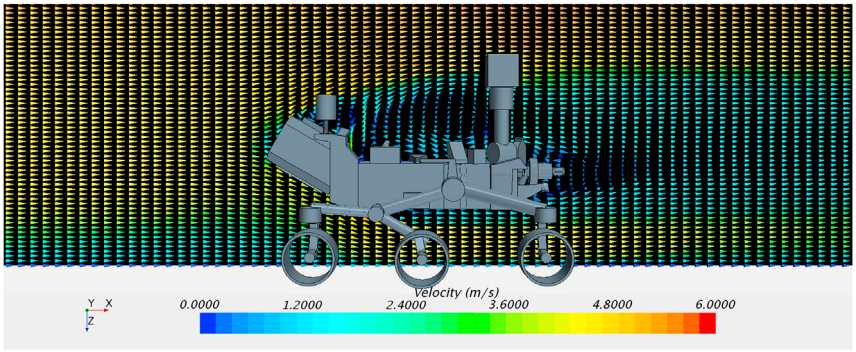

Fig. 31. Mean velocity vectors colored by velocity magnitude along the center-plane of the domain for $\theta = 0^{\circ}$ and $U(z_{ref}) = 5.0$ m/s for the rover with the turret in a stowed configuration.

In order to compare the cumulative amount of contaminant that is deposited on the surface with this new geometry, Figs. 19 and 20 are reproduced with the same y-axis limits, respectively, in Figs. 32 and 33. In general, it can be seen that the cumulative contaminant mass deposition is lower with the turret stowed when compared to the results with the turret deployed. From an operational stand point, it is much more likely that the rover will loiter near a sampling site with the turret deployed, and these results indicate that considering the turret deployed scenario is also a more conservative scenario for the predicted surface contaminant deposition values.

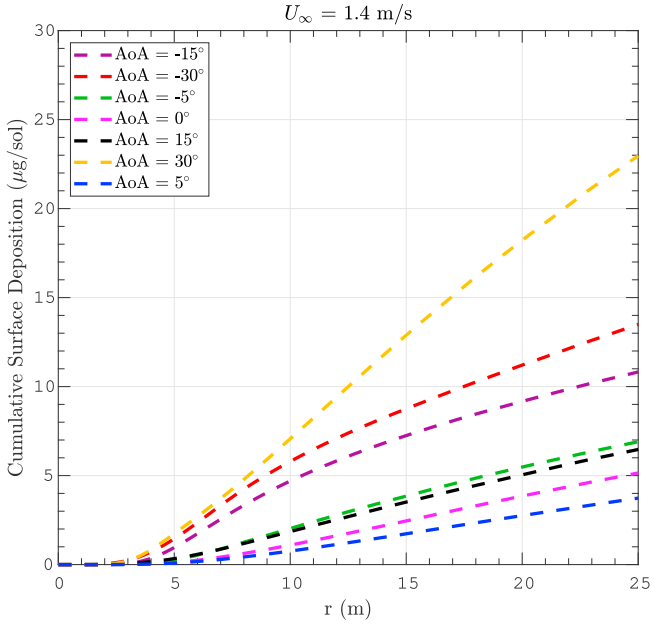

Fig. 32. Cumulative contaminant deposition profiles as a function of radius for $U(z_{ref}) = 1.4$ m/s.

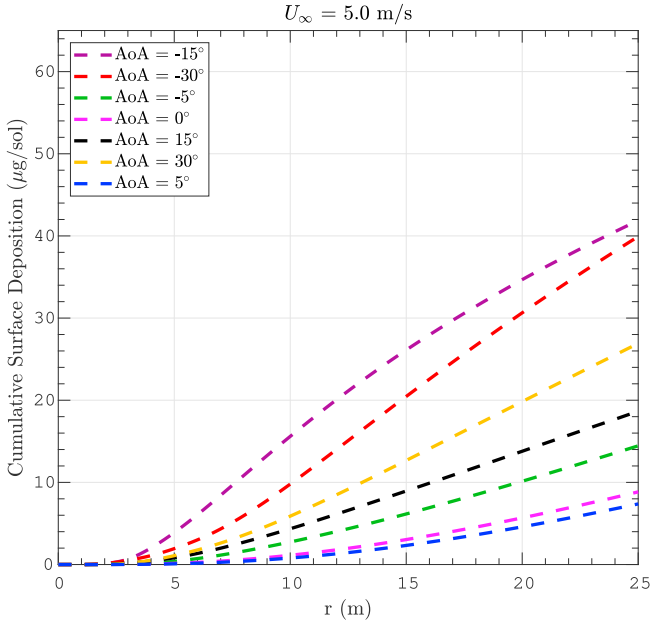

Fig. 33. Cumulative contaminant deposition profiles as a function of radius for $U(z_{ref}) = 5.0$ m/s.

The same spatial averaging technique that was described in Sec. IV.D is used to process the stowed turret results, and all results with the turret stowed predict a lower local maximum surface deposition when compared to the ~ 0.06 ng/cm^2/sol value shown in Fig. 24, which corresponds to the results with the turret deployed and $U(z_{ref}) = 5.0$ m/s, $\xi = -30^\circ$, and $\sigma = 15^\circ$. Fig 34 has the highest local maximum of surface max flux deposition (~ 0.045 ng/cm^2/sol) with the turret stowed, for $U(z_{ref}) = 5.0$ m/s, $\xi = -15^\circ$, and $\sigma = 15^\circ$. The local maximum surface flux value occurring for $\theta = -15^\circ$ is consistent with the cumulative mass deposition distributions shown in Fig. 33.

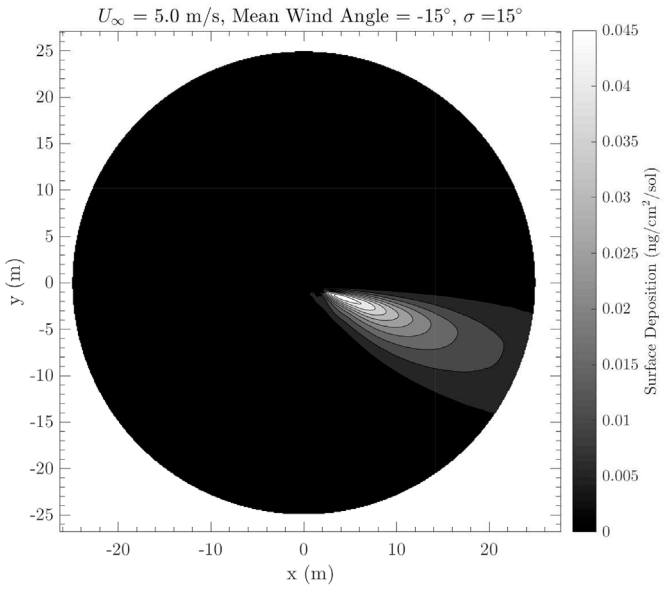

Fig. 34. Spatially averaged predicted contaminant surface mass deposition contour plot for $U(z_{ref}) = 5.0$ m/s, $\xi = -15^{\circ}$, and $\sigma = 15^{\circ}$.

References

Bird, R.B., Stewart, W.E., Lightfoot, E.N., 1960. Transport Phenomena. John Wiley & Sons.

Cucullu, G.C., Zayas, D., Novak, K., Wu, P., 2014. A curious year on Mars—long-term thermal trends for Mars Science Laboratory Rover's first Martian year. In: 44th International Conference on Environmental Systems, ICES-2014-295. https://ttu-ir.tdl.org/ttu-ir/handle/2346/59520.

Dimotakis, P.E., 2000. The mixing transition in turbulent flows. J. Fluid Mech. 409, 69–98. https://doi.org/10.1017/S0022112099007946.

Hess, S.L., Henry, R.M., Leovy, C.B., Ryan, J.A., Tillman, J.E., 1977. Meteorological results from the surface of mars: viking 1 and 2. J. Geophys. Res. 82 (28), 4559–4574. https://doi.org/10.1029/JS082i028p04559. https://doi.org/10.1029/JS082i028p04559.

Holzer, M., Siggia, E.D., 1994. Turbulent mixing of a passive scalar. Phys. Fluids 6 (5), 1820–1837. https://doi.org/10.1063/1.868243. https://doi.org/10.1063/1.868243.

Lienhard, J.H., 1966. Synopsis of Lift, Drag, and Vortex Frequency Data for Rigid Circular Cylinders, vol. 300. Technical Extension Service, Washington State University.

Lorenz, R.D., 1996. Martian surface wind speeds described by the Weibull distribution. J. Spacecraft Rockets 33 (5), 754–756.

Lorenz, R.D., 2016. Surface winds on Venus: probability distribution from in-situ measurements. Icarus 264, 311–315. https://doi.org/10.1016/j.icarus.2015.09.036. http://www.sciencedirect.com/science/article/pii/S0019103515004509.

Mahaffy, P.R., Webster, C.R., Atreya, S.K., Franz, H., Wong, M., Conrad, P.G., Harpold, D., Jones, J.J., Leshin, L.A., Manning, H., Owen, T., Pepin, R.O., Squyres, S., Trainer, M., MSL Science Team, 2013. Abundance and isotopic composition of gases in the martian atmosphere from the curiosity rover. Science 341 (6143), 263–266. https://doi.org/10.1126/science.1237966. http://science.sciencemag.org/content/341/6143/263.

Murphy, J.R., Leovy, C.B., Tillman, J.E., 1990. Observations of martian surface winds at the viking lander 1 site. J. Geophys. Res.: Solid Earth 95 (B9), 14555–14576. https://doi.org/10.1029/JB095iB09p14555. https://doi.org/10.1029/JB095iB09p14555.

Newman, C.E., Gómez-Elvira, J., Marin, M., Navarro, S., Torres, J., Richardson, M.I., Battalio, J.M., Guzewich, S.D., Sullivan, R., de la Torre, M., Vasavada, A.R., Bridges, N.T., 2017. "Winds measured by the rover environmental monitoring station (REMS) during the mars science laboratory (MSL) rover's bagnold dunes campaign and comparison with numerical modeling using MarsWRF. Icarus 291, 203–231. https://doi.org/10.1016/j.icarus.2016.12.016. http://www.sciencedirect.com/science/article/pii/S0019103516304699.

Novak, K.S., Kempenaar, J., Liu, Y., Bhandari, P., Lee, C.-J., 2013. Thermal performance of the mars science laboratory rover during mars surface operations. In: 43rd International Conference on Environmental Systems, AIAA 2013-3322.

Novak, K.S., Kempenaar, J.G., Redmond, M.J., Bhandari, P., 2015. Preliminary surface thermal design of the Mars 2020 Rover. In: 45th International Conference on Environmental Systems, ICES-2015-134, Bellevue, Washington.

Shraiman, B.I., Siggia, E.D., 2000. Scalar turbulence. Nature 405 (6787), 639. https://doi.org/10.1038/35015000. https://doi.org/10.1038/35015000.

Stern, S.A., Mullhaupt, J.T., Gareis, P.J., 1969. The effect of pressure on the permeation of gases and vapors through polyethylene. Usefulness of the corresponding states principle. AIChE J. 15 (1), 64–73. https://doi.org/10.1002/aic.690150117. https://onlinelibrary.wiley.com/doi/abs/10.1002/aic.690150117.

Summons, R., Sessions, A., Allwood, A., Barton, H., Beaty, D., Blakkolb, B., Canham, J., Clark, B., Dworkin, J., Lin, Y., Mathies, R., Milkovich, S., Steele, A., 2014. Planning considerations related to the organic contamination of martian samples and implications for the mars 2020 rover. Astrobiology 14 (12), 969–1027. https://doi.org/10.1089/ast.2014.1244. https://doi.org/10.1089/ast.2014.1244.

Warhaft, Z., 2000. Passive scalars in turbulent flows. Annu. Rev. Fluid Mech. 32 (1), 203–240. https://doi.org/10.1146/annurev.fluid.32.1.203. https://doi.org/10.1146/annurev.fluid.32.1.203.

White, L., Anderson, M., Blakkolb, B., Kipp, K., Stricker, M., Benardini, J.N., Mikellides, I., Katz, I., Bernard, D., Jandura, L., Rosette, K., Rainen, R., Steltzner, A., 2017. Organic and inorganic contamination control approaches for return sample investigation on Mars 2020. In: 2017 IEEE Aerospace Conference. https://doi.org/10.1109/AERO.2017.7943709.